

# High-temperature Tensile Properties and Creep Life Assessment of 25Cr35NiNb Micro-alloyed Steel

Amitava Ghatak  and P.S. Robi

(Submitted September 20, 2015; in revised form January 6, 2016; published online March 28, 2016)

Reformer tubes in petrochemical industries are exposed to high temperatures and gas pressure for prolonged period. Exposure of these tubes at severe operating conditions results in change in the microstructure and degradation of mechanical properties which may lead to premature failure. The present work highlights the high-temperature tensile properties and remaining creep life prediction using Larson-Miller parametric technique of service exposed 25Cr35NiNb micro-alloyed reformer tube. Young's modulus, yield strength, and ultimate tensile strength of the steel are lower than the virgin material and decreases with the increase in temperature. Ductility continuously increases with the increase in temperature up to 1000 °C. Strain hardening exponent increases up to 600 °C, beyond which it starts decreasing. The tensile properties are discussed with reference to microstructure and fractographs. Based on Larson-Miller technique, a creep life of at least 8.3 years is predicted for the service exposed material at 800 °C and 5 MPa.

**Keywords** creep and stress rupture, electron microscopy, fractography, HP40Nb stainless steel, life prediction, mechanical, x-ray

## 1. Introduction

Centrifugally cast 25Cr35NiNb micro-alloyed austenitic stainless steel (HP40Nb) is used as reformer tubes in petrochemical industries to withstand gas pressure of 1.5–5 MPa at temperatures above 800 °C and has been designed for a life of around 10<sup>5</sup> h (Ref 1–3). Mixture of vaporized naphtha and steam at 650 °C is feed from the top of the vertically placed reformer tubes which moves downward through the tubes. As the mixture moves down, at ~850 °C, they react, producing hydrogen-rich gas and the hydrogen-enriched gas mixture exit from the bottom of the tubes at around 930 °C. Prolonged service exposure degrades the microstructure and properties of the tubes, which many a times results in premature failure leading to forced shutdown of the plant. The high Cr and Ni content in the alloy results in precipitation and coarsening of carbides at grain boundaries during the prolonged exposure at high temperature leading to decrease in the creep strength (Ref 4, 5) of the tubes. Experimental studies have been carried out by various investigators to generate creep data of high-temperature metallic alloys. Attempts were also made to describe the creep behavior of these materials by constitutive models, continuum damage equations, omega method and  $\theta$  projection method, etc. (Ref 6–9). Since, reformer tubes operate in a severe environment for prolonged time period, the time- and temperature-dependent mechanical properties are useful parameters for the life assessment of these tubes during the design stage. Among the various parametric techniques,

Larson-Miller parameter ( $P_{L-M}$ ) (Ref 10) is the most commonly used method (Ref 11–15) for the creep life assessment of reformer tubes.  $P_{L-M}$  is expressed by the relationship

$$P_{L-M}(\sigma) = T(\log t_r + C_{L-M}) \times 10^{-3}, \quad (\text{Eq 1})$$

where  $C_{L-M}$  is the Larson-Miller constant,  $\sigma$  the stress,  $T$  the temperature, and  $t_r$  is the rupture time.

Although 25Cr35NiNb micro-alloyed steel is extensively used as reformer tubes in petrochemical industries, only limited information regarding high-temperature tensile properties, failure behavior, and stress rupture properties of this material is available in open literature (Ref 14–18). The present work is aimed at investigating tensile properties and fracture behavior at elevated temperature of 25Cr35NiNb micro-alloyed steel. The creep life assessment of the steel is also predicted using Larson-Miller parametric technique.

## 2. Methodology

### 2.1 Material

Centrifugally cast 25Cr35NiNb micro-alloyed austenitic stainless steel reformer tube supplied by Numaligarh Refineries Ltd., India, was used as the test material. The material was supplied in the form of tube with an inside diameter 106 mm, and thickness 15.3 mm was pre-exposed at 650 °C and pressure of 2.75 MPa for 11 years. The composition of the material analyzed by optical emission spectrometer is 0.4%C, 1.3%Si, 0.037%Mo, 23.6%Cr, 34.9%Ni, 0.8%Nb, 0.037%Ti, and balance Fe (in wt.%).

### 2.2 Sample Preparation

Flat tensile test specimens with 25 mm gage length and cross-sectional areas of 6.5 × 3 mm as per ASTM standard E8M-04 (Ref 19) were machined from the reformer tube by wire-cut electrical discharge machining (WEDM). The axis of the specimens was parallel to the longitudinal axis of the

Amitava Ghatak and P.S. Robi, Department of Mechanical Engineering, Indian Institute of Technology Guwahati, Guwahati, Assam 781039, India. Contact e-mail: a.ghatak@iitg.ernet.in.

reformer tube. These specimens were used for the high-temperature tensile tests as well as stress rupture tests.

### 2.3 High-temperature Tensile Test

Tensile tests were carried out using a 100 kN capacity INSTRON make, 8801 model servo hydraulic controlled universal testing machine (UTM). Prior to the test, the specimen was heated to the test temperature in a 2-zone resistance heated split furnace attached to the UTM. The furnace temperature was controlled by a PID controller with an accuracy of  $\pm 1$  °C. Tensile tests were carried out at room temperature as well as at elevated temperatures in the range of 200-1200 °C at an interval of 200 °C. After achieving the set temperature, the sample was soaked at the test temperature for further 10 min to ensure uniform temperature across the gage section. The specimen was monotonically loaded with a constant cross-head speed of 0.05 mm/min till failure. A high-temperature extensometer was used to measure the gage length extension during the tests. The load versus gage length extension data were recorded during each test. The stress-strain curves were obtained from the recorded data, and the Young's modulus ( $E$ ), yield strength (YS), ultimate tensile strength (UTS) and fracture strain values were determined. The true stress ( $\sigma$ )-true strain ( $\epsilon$ ) plots obtained was fitted with a Holloman-Ludwig power law equation of the form  $\sigma = K\epsilon^n$  (Ref 20). The strain hardening exponent ( $n$ ) was determined using the expression (Ref 21, 22)

$$n = \frac{d \log \sigma}{d \log \epsilon}_T \quad (\text{Eq 2})$$

### 2.4 Stress Rupture Test

Stress rupture tests were carried out following ASTM standard E-139 (Ref 23). The tests were carried out using an in-house developed constant true stress test set-up. The experiments were carried out at constant temperatures in the range 650-1050 °C and stress in the range 47-120 MPa. The specimen was heated to the test temperature by an impedance heater. The temperature of the specimen was measured by a non-contact infrared pyrometer and maintained constant till rupture within and accuracy of  $\pm 3$  °C. During the test, a high definition video camera was used to record the images of the specimen gage length extension till failure. Digital image frames from the video recording was extracted at regular time interval, and the time-dependent creep strain was determined by image processing technique. The creep life of the tube for any combination of temperature and stress was predicted by the Larson-Miller parametric technique using the expression (Ref 24, 25)

$$t_r = 10 \left[ \left( 1000 \times \frac{P_{L-M}}{T} \right) - C_{L-M} \right] \quad (\text{Eq 3})$$

The creep life of the tube predicted is corresponding to the hoop stress ( $\sigma_h$ ) of the tube during the service application of the reformer tube. The hoop stress acting on the tube was determined using the following relation (Ref 26):

$$\sigma_h = \frac{Pd}{2t}, \quad (\text{Eq 4})$$

where  $P$  is the operating pressure of fluid in MPa,  $d$  is the inner diameter in mm, and  $t$  is the thickness of the tube in mm. Based on the service conditions, the hoop stress was determined as  $\sim 5$  MPa.

### 2.5 Microstructure and Fractography

Microstructure of the as-received material was characterized using LEO 1430VP SEM (Carl Zeiss, Germany) attached with an energy dispersive x-ray spectroscopy (EDS) system. The fracture surfaces of the tensile tested samples were observed under the SEM to investigate the mechanism of tensile fracture in this steel. The longitudinal sections of the failed tensile specimen were machined by WEDM. The as-received and longitudinal sectioned samples were polished for microstructural investigation following the standard metallographic specimen preparation techniques. The samples were mounted in thermos-setting resin using a hot mounting press. These were then ground with a series of SiC papers followed by micro polishing using alumina suspension. The polished samples were etched using Glyceregia solution (15 mL hydrochloric acid, 10 mL glycerol and 5 mL nitric acid), and microstructural investigations were carried out using an upright optical microscope. The polished sample in the un-etched condition was analyzed by SEM, and the compositions of various phases were determined by EDS.

### 2.6 X-ray Diffraction Technique

The various phases present in the steel was determined by x-ray diffraction (XRD) technique. To determine the phases present at high temperature, the steel was heat treated at 1000 °C for 2 h and quenched in water. The as-received as well as the heat treated sample were dissolved in Glyceregia solution and filtered. The filtrand powders were analyzed using Bruker D8 x-ray diffractometer.

## 3. Results and Discussion

### 3.1 Microstructure

Figure 1 shows the SEM micrograph of the as-received steel. The microstructure shows network of carbide precipitates at grain boundary regions. Three types of carbides are observed. The dark gray carbide precipitates (phase-A) and white precipitates (phase-B) are identified as Cr-rich carbide and Nb-rich carbides, respectively, whereas the fine white

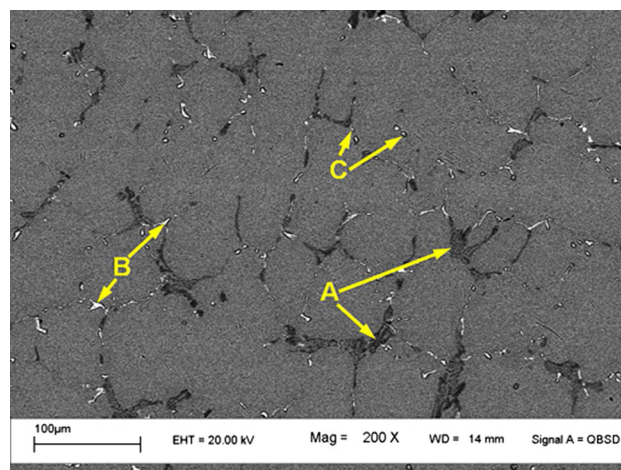


Fig. 1 SEM micrograph of the as-received steel

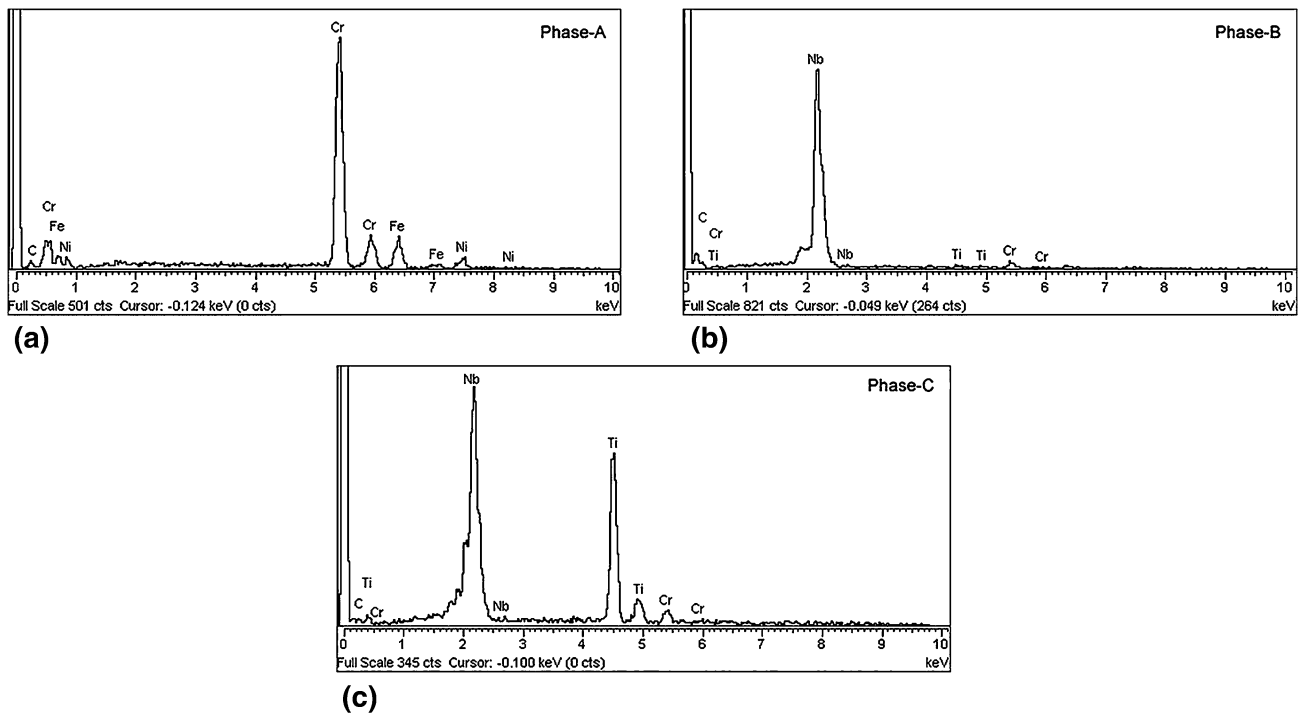


Fig. 2 EDS spectrum of (a) phase-A, (b) phase-B, and (c) phase-C

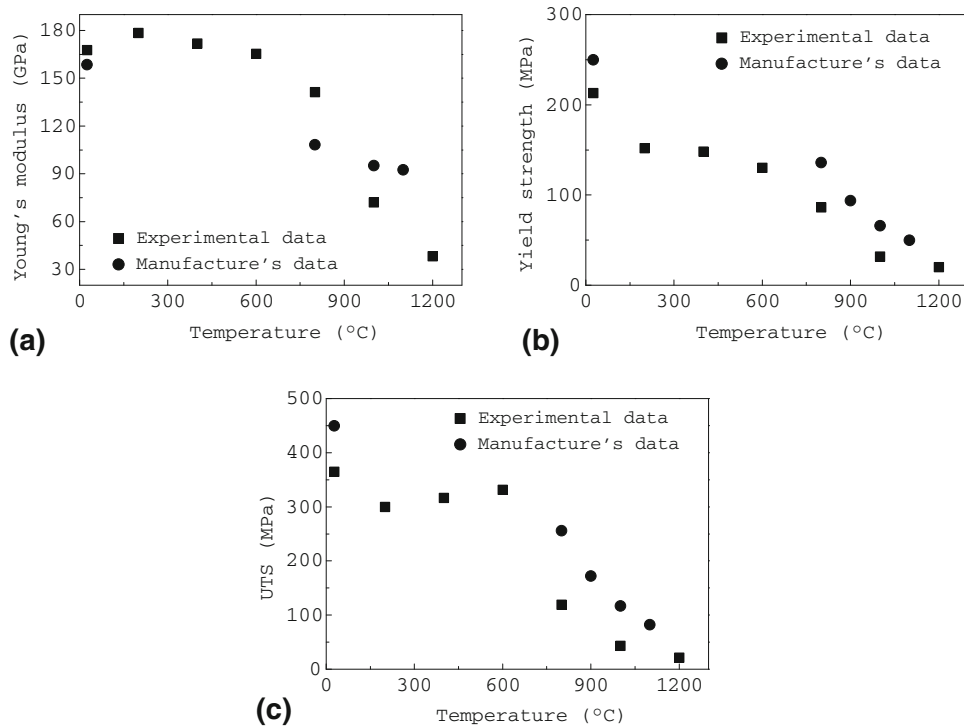


Fig. 3 (a) Plots of Young's modulus, (b) yield strength, and (c) ultimate tensile strength vs. temperature

precipitates (phase-C) are identified as Nb-Ti-rich carbide. Figure 2(a)-(c) shows EDS spectrum of the three types of carbide precipitates. No evidence of any microscopic defects in the form of void, cavitation, or crack was observed during the investigation.

### 3.2 Tensile Properties

Figure 3(a)-(c) shows the plots of  $E$ , YS, and UTS versus temperature for the steel, respectively. Due to unavailability of standard data, the test results are compared with the values

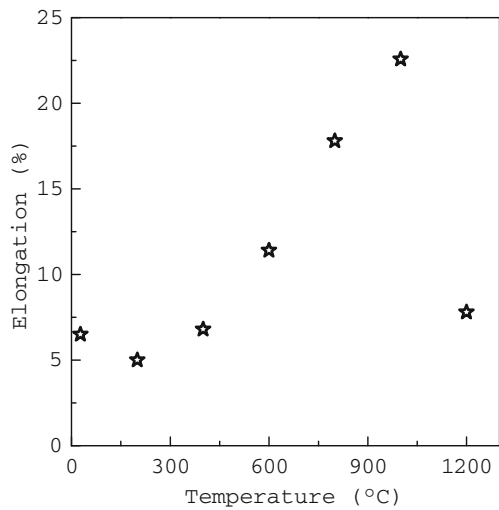


Fig. 4 Plot of percentage elongation vs. temperature

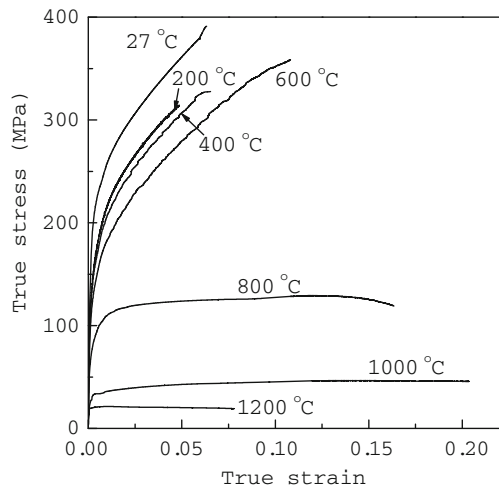


Fig. 5 True stress-true strain curves at various test temperatures

reported by the manufacturer (Ref 27) for the as-cast material. The  $E$  versus temperature plot shown in Fig. 3(a) indicates a marginal decrease in Young's modulus values as the test temperature was raised from 27 to 600 °C. For test temperatures in the range from 600 to 1200 °C, a rapid and continuous decrease in  $E$  value is evident with increase in temperature. The  $E$  value of the service exposed material is higher than that of the as-cast material for temperature up to 800 °C. Above 800 °C, the  $E$  value of the as-cast material is higher than service exposed tube. Figure 3(b) and (c) indicates that the yield strength and ultimate tensile strengths for the service exposed steel was lower than the as-cast material at all test temperatures. The yield strength decreases continuously with the increase in temperature. The ultimate tensile strength (UTS) shows a decreasing trend only above 600 °C. The UTS of the steel was decreased by 94% when the test temperature was increased from 600 to 1200 °C. At 1000 °C, the  $E$ , YS, and UTS values of the service exposed steel decreased by 24, 51, and 64%, respectively, compared to the manufacturer's data. The results indicate degradation in the tensile properties of the reformer

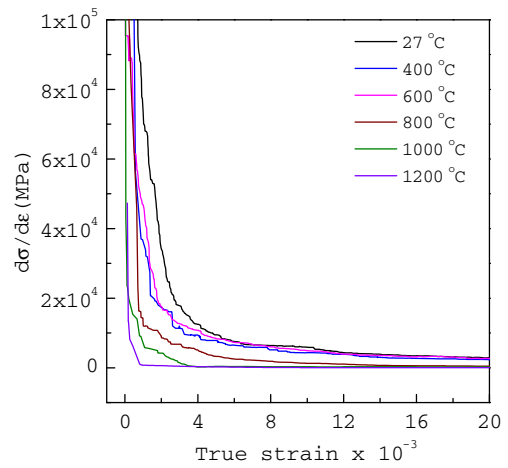


Fig. 6 Plot of  $\frac{d\sigma}{d\epsilon}$  vs.  $\epsilon$  up to a strain of 0.02

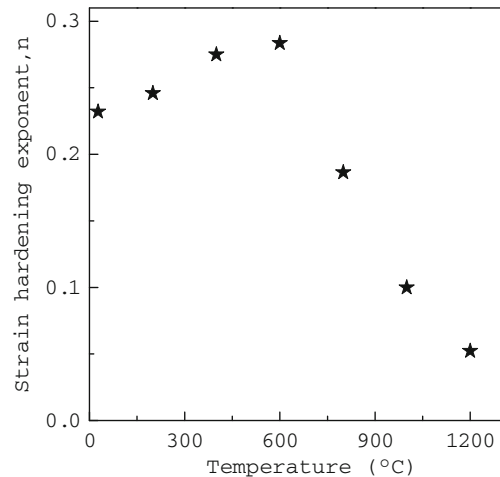


Fig. 7 Plot of strain hardening exponent vs. temperature

tube due to the exposure at 650 °C for 11 years, though there was no evidence of any microstructural degradation.

Figure 4 shows the percentage elongation versus temperature plot for the steel indicating low ductility at lower temperatures. The ductility varied only marginally up to 400 °C. The ductility increased from 6.7 to 22.6% as the temperature was increased from 400 to 1000 °C. With further increase in test temperatures, the ductility decreased drastically to 7.8% at 1200 °C, indicating sharp loss of ductility above 1000 °C.

The true stress-true strain ( $\sigma$ - $\epsilon$ ) plots obtained for the steel at various test temperatures is presented in Fig. 5. The flow stress of the steel is strongly dependent on the test temperature. The onset of plastic deformation is accompanied by high strain hardening rate ( $d\sigma/d\epsilon$ ). Up to a test temperature of 600 °C, the material strain hardened continuously till failure. At a test temperature of 800 °C, the onset of plastic deformation was accompanied by a strain hardening region up to a true strain of around 0.015, beyond which effectively no strain hardening was observed. With further straining, the material undergoes a

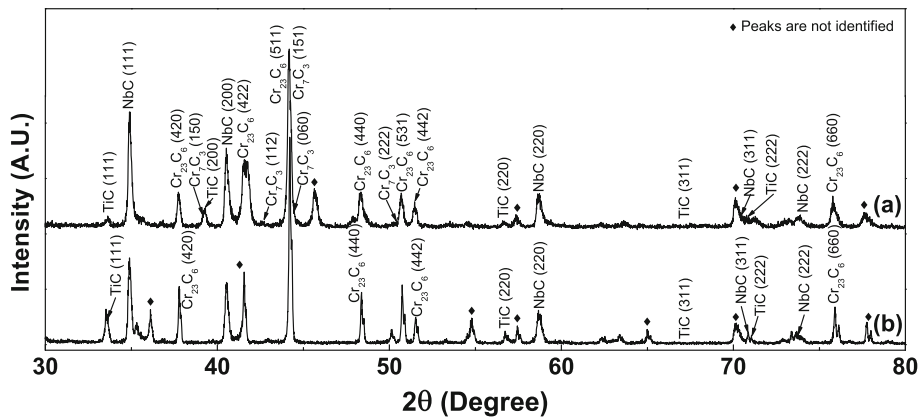


Fig. 8 XRD pattern of the steel heat affected at (a) 650 °C and (b) 1000 °C

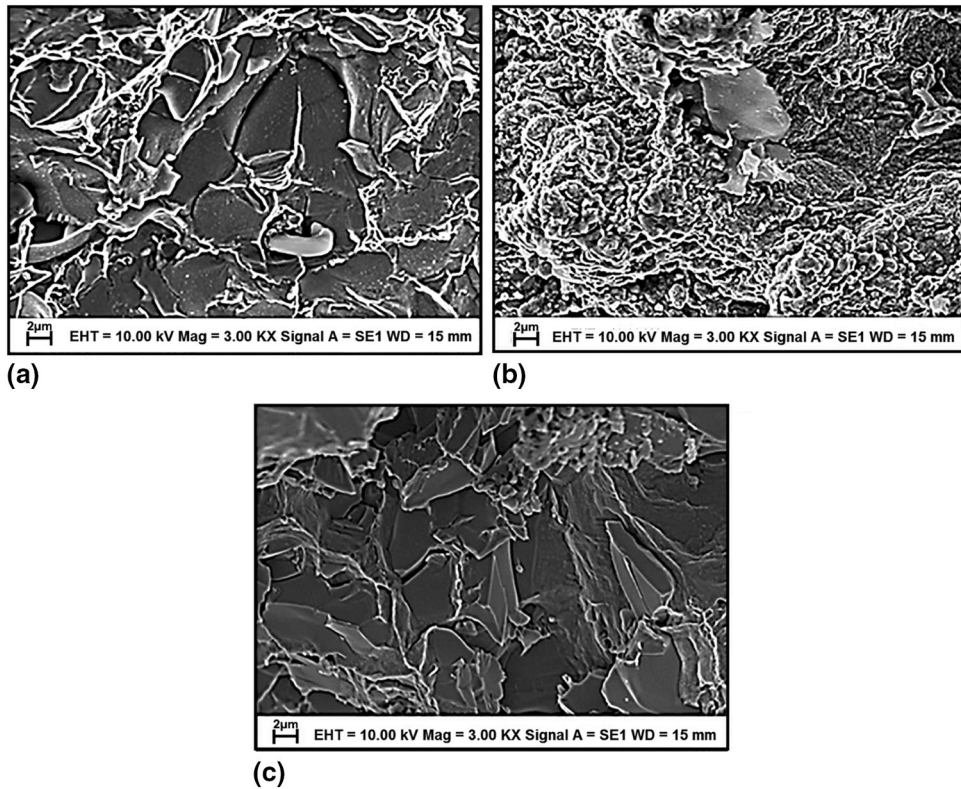


Fig. 9 SEM fractographs of HP40Nb steel tested at (a) 27 °C, (b) 800 °C, and (c) 1200 °C

large amount of plastic deformation at almost a constant stress, prior to failure. At 1000 °C, the material behavior was as if perfectly plastic material. The true plastic strain to failure at 1000 °C was 0.21. Above 1000 °C, though the behavior of the steel was perfectly plastic, it was also characterized by sharp loss in ductility. At 1200 °C, the yield strength of the material was 20 MPa with a true strain to failure value of 0.075.

Figure 6 shows the  $d\sigma/d\varepsilon$  versus  $\varepsilon$  plot of the material for different test temperatures, indicating high strain hardening rate at the onset of plastic deformation. The strain hardening rate decreased with increase in strain, and beyond a certain strain, the strain hardening rate saturates at certain minimum values.

Above 600 °C, the strain hardening rate at the onset of plastic deformation was lower. At a strain of 0.015, the strain hardening rate at 800, 1000, and 1200 °C were 636, 294, and 45 MPa, respectively. It is also observed that minimum strain hardening rate decreased with increase in temperature. Above 600 °C, the strain hardening was observed only for a very small amount of strain, indicating that the material deformed as if an almost perfectly plastic material.

Figure 7 shows the strain hardening exponent versus temperature ( $n$  versus  $T$ ) plot. The  $n$  value increases with the increase in test temperatures up to 600 °C. After reaching a maximum value of 0.284, the  $n$  value decreases sharply with

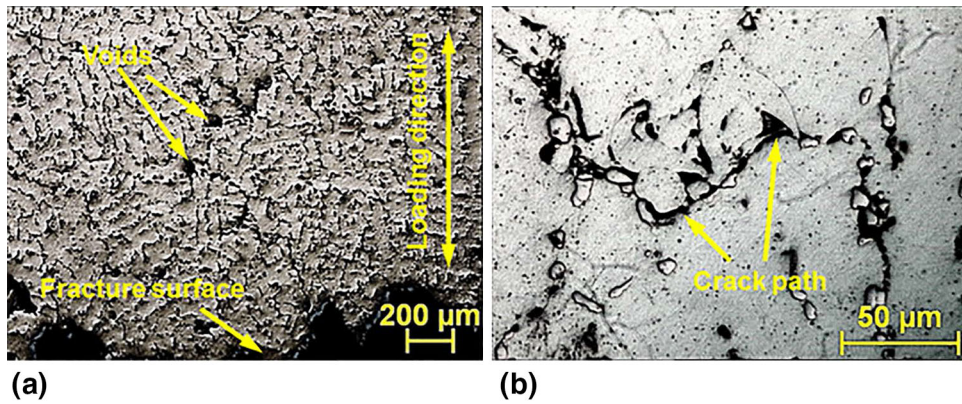


**Fig. 10** Optical micrographs of longitudinal section HP40Nb steel tested at 1200 °C observed at (a) low magnification and (b) high magnification

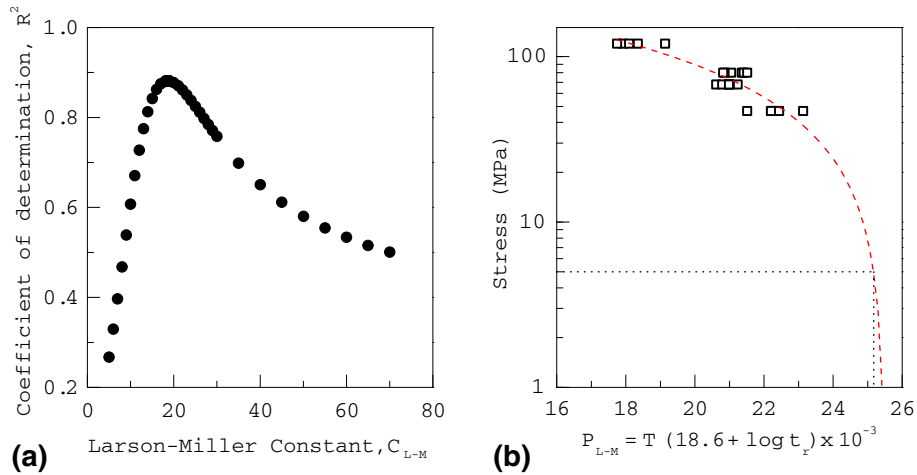


**Fig. 11** (a) Variation of  $R^2$  with  $C_{L-M}$  for linear fit of Eq 1 and (b) stress vs.  $P_{L-M}$  master curve plot of the steel

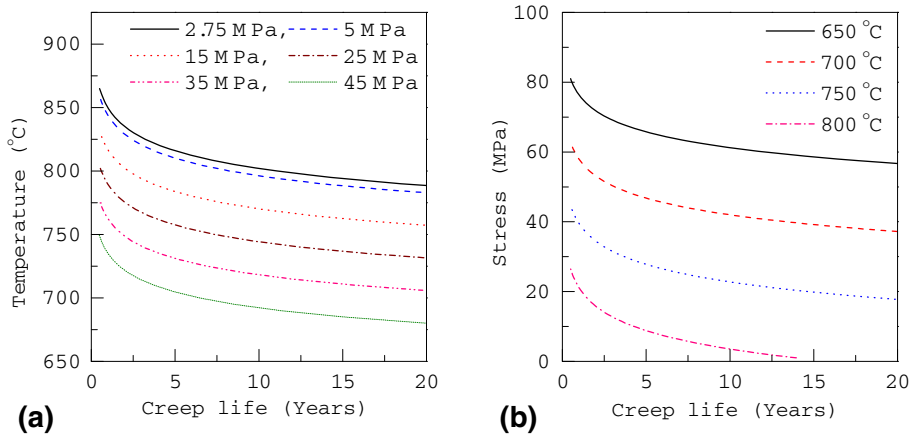


**Fig. 12** (a) Temperature-creep life and (b) stress-creep life plot for the service exposed steel

the increase in test temperature. At 1200 °C, the value of  $n$  was determined to be 0.05 which indicates negligible work hardening. However, at this temperature, the strain to failure was found to be very low. The degradation of tensile properties

(viz.  $E$ ,  $Y_S$ ,  $U_{TS}$ ) of the service exposed reformer tube compared to the as-cast tube material, indicates that the material has softened due to prolonged exposure at service temperature and pressure.

### 3.3 XRD Analysis

Figure 8(a) and (b) shows the XRD patterns obtained from the powders of the as-received and heat treated steel, respectively. Figure 8(a) reveals the presence of second phase particles of  $\text{Cr}_7\text{C}_3$ ,  $\text{Cr}_{23}\text{C}_6$ , NbC, and TiC. The XRD pattern of the powder obtained from the heat treated samples shown in Fig. 8(b) does not reveal the presence of  $\text{Cr}_7\text{C}_3$  particles. This indicates the dissolution of  $\text{Cr}_7\text{C}_3$  in the matrix during the heat treatment at elevated temperature.

The sharp decrease in strength and Young's modulus for the material at elevated temperatures can be attributed to the dissolution of the second phase  $\text{Cr}_7\text{C}_3$  particles in the matrix. During the application of stress, the presence of fine particles acts as barriers for the dislocation movement along the slip planes, thereby increasing the strength of the material. These particles can either act as strong impenetrable particles through which dislocations can move or they can act as coherent particles through which dislocations can pass. In the former case, the dislocations can move by changing the curvature of the dislocation line, whereas in the latter case, the dislocations can pass through the particles only at stress levels much above those required to move the dislocations through the matrix. At temperatures above 650 °C, the dissolution of  $\text{Cr}_7\text{C}_3$  particles in the matrix with concomitant increase in  $\text{Cr}_7\text{C}_3$  results in less resistance for the dislocation motion along the slip planes, resulting in the decrease in strength and increase in ductility. Formation of the  $\text{Cr}_{23}\text{C}_6$  precipitates at the grain boundary leads to a decrease in chromium concentration in the matrix resulting in less distortion of the matrix, lattice which also decreases the alloy strength with decrease in chromium concentration in matrix (Ref 28). Beyond 1000 °C, the flow strength of the matrix reduces drastically, which results in the nucleation of micro voids at the matrix- $\text{Cr}_{23}\text{C}_6$  interface regions resulting in failure by intergranular fracture.

### 3.4 Fractography

Figure 9(a)-(c) shows the SEM fractographs of the specimen tensile tested at different temperatures. At 27 °C, the specimen fails in a brittle manner as evident from the cleavage features, Fig. 9(a). The figure reveals features of particle fracture and debonding at the particle-matrix interface. Similar features are observed in samples tested at temperatures up to 600 °C. Figure 9(b) shows the fractograph of the sample tested at 800 °C indicating ductile features. The features indicate transgranular failure due to extensive plastic deformation of the grains before final failure. Since, the microstructure of the material revealed carbides present at grain boundary regions, during the tensile loading at temperatures up to 1000 °C, the main mechanism of failure is due to the deformation of the grains by multiple slip rather than by micro-void coalescence. Figure 9(c) shows SEM fractograph of the sample tested at 1200 °C, indicating intergranular failure. The fracture features indicate voids at particle-matrix interface, especially at grain boundary regions.

Figure 10(a) and (b) shows the optical micrographs at lower and higher magnification, respectively, of the polished surface of longitudinally sectioned sample tested at 1200 °C. Low-magnification micrograph reveals creep cavities or voids near the fracture surface. Higher-magnification micrograph shows nucleation of creep cavities at carbide-matrix interfaces in grain boundary regions. The carbide precipitates at grain boundary

regions are found in the form of discontinuous particles. At higher temperature, carbon atom diffuses from the Cr-rich carbide ( $\text{Cr}_{23}\text{C}_6$ ) to the Nb- and Ti-rich carbides resulting in a change in the morphology of the grain boundary carbide network. Similar feature was reported by Ghatak et al. (Ref 29). Figure 10(b) also reveals that the propagation of the voids is along grain boundary regions. Thus, it can be concluded that the low ductility exhibited by this steel at 1200 °C is due to intergranular failure.

### 3.5 Creep Life Assessment

Larson-Miller parameter is widely accepted by industries to predict creep life of materials. The master curve for the Larson-Miller parametric technique is the plot of  $\sigma$  versus  $P_{L-M}$ . The relationship between the stress and  $P_{L-M}$  can be expressed as (Ref 24)

$$\sigma = a_0 + a_1 P_{L-M}, \quad (\text{Eq 5})$$

where  $a_0$  and  $a_1$  are constants. The  $P_{L-M}$  values were found to be different when the different values of  $C_{L-M}$  are used in Eq 1. The plot of best  $\sigma$  versus  $P_{L-M}$  master curve is obtained when the optimum value of  $C_{L-M}$  was chosen. The optimum value of  $C_{L-M}$  corresponds to the case where coefficient of determination  $R^2$  is maximum for the linear fit of the stress  $\sigma$  versus  $P_{L-M}$  master curve. Figure 11(a) shows the variation of  $R^2$  value obtained by varying  $C_{L-M}$  value by trial and error. From this plot, the best fit is obtained for a  $C_{L-M}$  value of 18.6 where  $R^2 = 0.882$ . The corresponding values of constants  $a_0$  and  $a_1$  in Eq 5 are, respectively, 416.276 and  $-16.339$ . Figure 11(b) shows the semi-log plot of  $\sigma$  versus  $P_{L-M}$  for the reformer tube indicating a linear relationship between  $\sigma$  and  $P_{L-M}$ .

The  $P_{L-M}$  value for stresses outside the domain of investigation is obtained by linear extrapolation of the master curve to low stress values. The extrapolated values of  $P_{L-M}$  were determined for the stresses in the range 2.75-45 MPa of the service exposed reformer tube. The creep life of the reformer tube corresponding to the optimum value of  $C_{L-M}$  (=18.6) is given by Eq 6:

$$t_r = 10^{[(1000 \times \frac{P_{L-M}}{T}) - 18.6]}. \quad (\text{Eq 6})$$

Figure 12(a) and (b) shows the remaining life of the reformer tube at constant stresses and temperatures, respectively. The figures indicate decrease in creep life with the increase in temperature and stress, respectively. At 800 °C/ 2.75 MPa and 800 °C/5 MPa the creep life of the steel is 11.9 and 8.3 years, respectively.

No evidence of creep degradation like creep voids or cavities was observed (Fig. 1) during the microstructural investigation. Typically in reformer steel tubes, creep cavities nucleate at the onset of tertiary stage. It is unrealistic to perform creep experiment for the exact service life of the material since that would take almost more than a decade of uninterrupted test. The master plot of  $\sigma$  versus  $P_{L-M}$  (Fig. 11b) is a graphical representation of short-time creep test data. The creep rupture time for any combination of stress and temperature is generally determined by extrapolating the master curve. The tube for the present study was service exposed at 650 °C for 11 years. Extrapolation of the master curve (Fig. 11b) shows a creep rupture time of several decades at 650 °C/5 MPa, indicating only marginal degradation due to the service exposure. The result reveals that the service exposed reformer tube can be

used for further use. Creep life analysis reveals that at 5 MPa stress, the remaining creep life for this steel is 8.3 years and 12 months at 800 and 850 °C, respectively, indicating that the creep life decreases rapidly with increase in temperature. By judiciously choosing the temperature and stress, the service exposed steel can be further used for a life of 10<sup>5</sup> h.

## 4. Conclusion

The microstructure of the as-received material consisted of Cr<sub>7</sub>C<sub>3</sub>, Cr<sub>23</sub>C<sub>6</sub>, NbC, and TiC phases at the austenite grain boundaries. Young's modulus, yield strength, and ultimate tensile strength of the steel decreased and percentage elongation increased with the increase in temperature. The strain hardening exponent of the steel increased with the increase in temperature up to 600 °C and decreased with the further increase in temperature. Dissolution of Cr<sub>7</sub>C<sub>3</sub> particles at elevated temperature resulted in the sharp decrease in strength of the steel. Up to 600 °C, the failure of the material was by brittle fracture. Between 600 and 1000 °C, failure was by multiple slip, whereas at 1200 °C, it was by intergranular fracture. Analysis by Larson-Miller parametric technique revealed the remaining life of the service exposed steel as 8.3 years at 800 °C and 5 MPa.

## Acknowledgments

The authors acknowledge Numaligarh Refineries Limited, India for providing the reformer tube necessary for the work. The authors are also grateful to Central Instruments Facility, IIT Guwahati, India for extending the SEM facility.

## References

1. C.W. Briggs, *Steel Castings Handbook*, 4th ed., Steel Founders' Society of America, Crystal Lake, 1970
2. A. Alvino, D. Lega, F. Giacobbe, V. Mazzocchi, and A. Rinaldi, Damage Characterization in Two Reformer Heater Tubes After Nearly 10 Years of Service at Different Operative and Maintenance Conditions, *Eng. Fail. Anal.*, 2010, **17**, p 1526–1541
3. T.C. Chou, W. Huang, and R. Paciej, Stress Corrosion Cracking of Pyrotherm Reformer Tube for Steam-Reforming Hydrogen Production, *J. Mater. Sci.*, 1997, **32**, p 67–72
4. J.M. Joubert, W. St-Fleur, J. Sarthou, A. Steckmeyer, and B. Fournier, Equilibrium Characterization and Thermodynamic Calculations on Highly Alloyed Refractory Steels, *Calphad*, 2014, **46**, p 55–61
5. C.J. Liu and Y. Chen, Variations of the Microstructure and Mechanical Properties of HP40Nb Hydrogen Reformer Tube with Time at Elevated Temperature, *Mater. Des.*, 2011, **32**, p 2507–2512
6. L.T. Li, Y.C. Lin, H.M. Zhou, Y.C. Xia, and Y.Q. Jiang, Modeling the High-Temperature Creep Behaviors of 7075 and 2124 Aluminum Alloys by Continuum Damage Mechanics Model, *Comput. Mater. Sci.*, 2013, **73**, p 72–78
7. A. Ghatak and P.S. Robi, A Comparative Study of Constitutive Equations for the Creep Deformation of HP40Nb Micro-alloyed Steel, *Mater. Sci. Eng. A*, 2015, **648**, p 418–427
8. A. Ghatak and P.S. Robi, High-Temperature Deformation Behavior of HP40Nb Micro-alloyed Reformer Steel, *Metallogr. Microstruct. Anal.*, 2015, **4**, p 508–517
9. Y.C. Lin, Y.Q. Jiang, H.M. Zhou, and G. Liu, A New Creep Constitutive Model for 7075 Aluminium Alloy Under Elevated Temperatures, *J. Mater. Eng. Perform.*, 2014, **23**, p 4350–4357
10. F.R. Larson and J. Miller, A Time-temperature Relationship for Rupture and Creep Stresses, *Trans. ASME*, 1952, **74**, p 765–771
11. J. Dong, K. Shin, K.C. Kim, and B.H. Kim, Precipitates in 9-12% Cr Steel After Creep Rupture Test and Determination of Life Time Assessment upon Larson-Miller Parameter, *Adv. Sci. Lett.*, 2011, **4**, p 2555–2559
12. A.H.D. Sorkhabi and F.V. Tahami, Creep Constitutive Equation for 2-Materials of Weldment-304L Stainless Steel, *World Acad. Sci. Eng. Technol.*, 2012, **61**, p 710–714
13. A.K. Ray, K. Diwakar, B.N. Prasad, Y.N. Tiwari, R.N. Ghosh, and J.D. Whittenberger, Long Term Creep-rupture Behaviour of 813 K Exposed 2.25-1Mo Steel Between 773 and 873 K, *Mater. Sci. Eng. A*, 2007, **454–455**, p 124–131
14. J.E. Indacochea and R.A. Seshadri, An Analysis of Creep Damage in a Welded Low Alloy Steel Rotor, *Mater. Sci. Eng. A*, 1997, **234–236**, p 555–558
15. A.K. Ray, S. Kumar, G. Krishna, M. Gunjan, B. Goswami, and S.C. Bose, Microstructural Studies and Remnant Life Assessment of Eleven Years Service Exposed Reformer Tube, *Mater. Sci. Eng. A*, 2011, **529**, p 102–112
16. J. Swaminathan, K. Guguloth, M. Gunjan, P. Roy, and R. Ghosh, Failure Analysis and Remaining Life Assessment of Service Exposed Primary Reformer Heater Tubes, *Eng. Fail. Anal.*, 2008, **15**, p 311–331
17. E. Hamzah, M. Mudang, A.K. Jenq, and M.A. Khattak, High Temperature Creep Behavior of Austenitic Fe-Ni-Cr alloy, *Adv. Mater. Res.*, 2013, **686**, p 170–179
18. A.K. Ray, S.K. Sinha, Y.N. Tiwari, J. Swaminathan, G. Das, S. Chaudhuri, and R. Singh, Analysis of Failed Reformer Tubes, *Eng. Fail. Anal.*, 2003, **10**, p 351–362
19. ASTM E8M-04, *Standard Test Methods for Tension Testing of Metallic Materials (metric) (Annual Book of ASTM Standards)*, ASTM, West Conshohocken, 2004
20. S. Surendarnath, K. Sankaranarayanan, and B. Ravisankar, Workability Study on 99.04% Pure Aluminium Processed by ECAP, *Mater. Manuf. Process.*, 2014, **29**, p 691–696
21. J. Luo and M.Q. Li, Strain Rate Sensitivity and Strain Hardening Exponent During the Isothermal Compression of Ti60 Alloy, *Mater. Sci. Eng. A*, 2012, **538**, p 156–163
22. J. Deng, Y.C. Lin, J. Chen, S.S. Li, and Y. Ding, Hot Tensile Deformation and Fracture Behaviors of AZ31 Magnesium Alloy, *Mater. Des.*, 2013, **49**, p 209–219
23. ASTM 139, *Standard Test Methods for Conducting Creep, Creep-Rupture, and Stress-Rupture Tests of Metallic Materials*, ASTM, West Conshohocken, 2003
24. A. Ghatak and P.S. Robi, Investigation of Micro-structure and Creep Life Analysis of Centrifugally Cast Fe-Cr-Ni Alloy Reformer Tubes, *Manuf. Sci. Technol.*, 2015, **3**, p 155–159
25. A. Ghatak and P.S. Robi, Creep behavior and creep life assessment of HP40Nb reformer steel, *Int. J. Res. Eng. Appl. Sci.*, 2015, **5**, p 98–105
26. R.K. Bansal, *A Textbook of Strength of Materials*, 4th ed., Laxmi Publications (P) Ltd., New Delhi, 2010, p 749
27. H39WM, *25/35 Cr/Ni Nb 0.4% C Microalloy Cast Heat Resisting Alloy, Physical Properties*, Doncasters Paralloy Ltd, Billingham, 2013
28. A.K. Jena and M.C. Chaturvedi, The Role of Alloying Elements in the Design of Nickel-Base Superalloys, *J. Mater. Sci.*, 1984, **19**, p 3121–3139
29. A. Ghatak and P.S. Robi, Effect of Temperature on the Microstructure and Hardness of Service Exposed 25Cr35NiNb Reformer Tubes, *Trans. Indian Inst. Met.*, 2016, **69**, p 823–827